Water Science & Technology

Water Science & Technology Vol 84 No 4, 1011 doi: 10.2166/wst.2021.248

New green electrode materials derived from waste cigarette butts for capacitive deionization

Ying Yang[a], Shudi Mao[a], Zhe Li[a], Zhuo Sun[a,b] and Ran Zhao[a,b,*]
[a] Engineering Research Center for Nanophotonics & Advanced Instrument, Ministry of Education, School of Physics and Electronic Science, East China Normal University, 500 Dongchuan Road, 200241 Shanghai, China
[b] East China Normal University-University of Alberta Joint Institute of Advanced Science and Technology, 500 Dongchuan Road, 200241 Shanghai, China
*Corresponding author. E-mail: rzhao@phy.ecnu.edu.cn

RZ, 0000-0003-3250-4505

ABSTRACT

Smoked cigarette butts are a non-biodegradable pollutant that has damaged the planet. However, carbon materials derived from cigarette butts have proven to be suitable for various applications. We synthesized cigarette butt-derived carbon via hydrothermal carbonization and chemical activation methods and then converted it to an electrode material for capacitive deionization. The fabricated material, SCC-750, exhibited a relatively high salt adsorption capacity of 10.27 mg g^{-1}. The excellent CDI (capacitive deionization) performance is due to the high specific surface area of 3,093.10 m^2 g^{-1} and a pore volume of 1.754 cm^3 g^{-1}. This work offers a new method to recycle harmful cigarette butts by converting them into promising electrode materials for capacitive deionization.

Key words: capacitive deionization, carbon material, cigarette butt, hydrothermal carbonization, porous structure

HIGHLIGHTS

- Explore the influence of chemical activation temperature and compare the capacitive deionization performance of the carbon material derived from smoked cigarette butts and unsmoked cigarette butts.
- Smoked cigarette butt-derived carbon at the activation temperature of 750 °C exhibits high specific surface area of 3,093.10 m^2 g^{-1}, high pore volume of 1.75 cm^3 g^{-1}, and reaches a high salt adsorption capacity 10.27 mg g^{-1}.

GRAPHICAL ABSTRACT

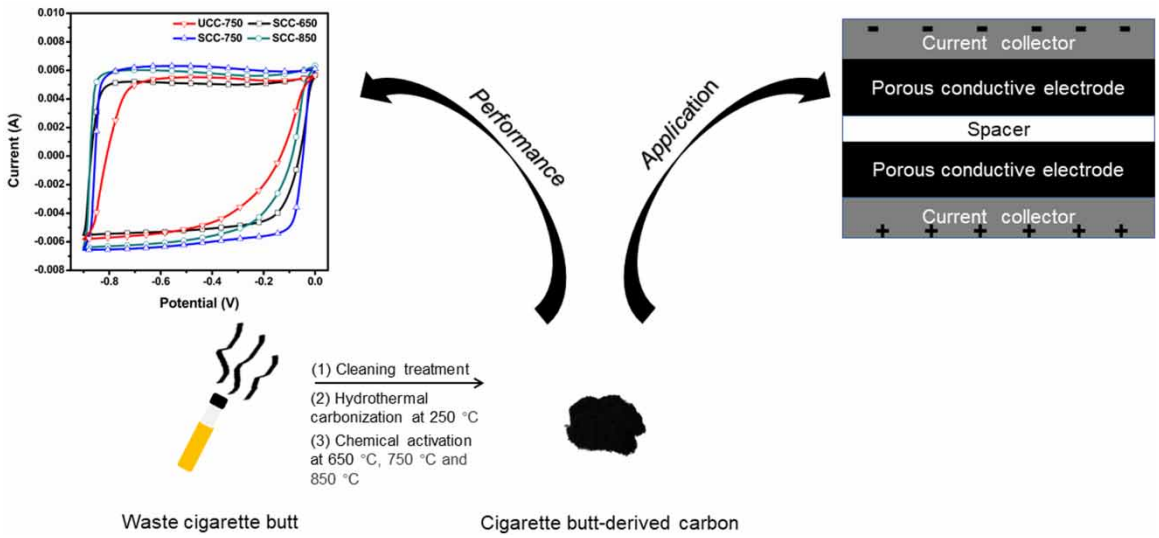

1. INTRODUCTION

Water shortage has become a global strategic concern to all human survival due to the rapidly growing population and developing industries (Vörösmarty *et al.* 2010; Naimi Ait-Aoudia & Berezowska-Azzag 2016; Sutcliffe *et al.* 2021). For example, more than 75% of Chinese cities are suffering from water shortages (Hou *et al.* 2021). It has been predicted that at least 25% of the population may live under water scarcity by 2050 (Hou *et al.* 2021), which emphasizes the urgent demand for sufficient clean water. Desalination of saline water is considered one of the feasible strategies to tackle this issue (Biesheuvel *et al.* 2011; He *et al.* 2018; Zhang *et al.* 2019a).

Current desalination techniques include reverse osmosis, thermal distillation, and electrodialysis. These all inevitably have some drawbacks such as high energy cost, the need for subsequent remineralization, and secondary pollution (Strathmann 2010; Porada *et al.* 2013; Suss *et al.* 2015). Capacitive deionization (CDI) is advantageous because of the cost-efficiency, high-water recovery ratio, and facile operation compared to the former methods (Mao *et al.* 2019; Zhang *et al.* 2019b; Vafakhah *et al.* 2020; Li *et al.* 2021). The ions or polar molecules in the saline stream will be adsorbed to the electrical double layers (EDLs) of their counter electrodes with application of an electrical potential difference in CDI. Normally, a 1.23 V or less bias is needed to desalinate water (Porada *et al.* 2013). The cell can then be short-circuited to regenerate the electrodes (Porada *et al.* 2013). Increasing the salt adsorption capacity is crucial to improve the performance of CDI (Biesheuvel *et al.* 2011). Therefore, one of the most effective research angles is to seek better electrode materials (Anderson *et al.* 2010; Zhao *et al.* 2020). High specific surface area (SSA), favorable pore size distribution, high stability, and high conductivity are the key factors to consider (Jia & Zhang 2016; Gao *et al.* 2021; Li *et al.* 2021). Carbon materials such as activated carbon (Ghaffour *et al.* 2013; Asquith *et al.* 2015), carbon nanotubes (Zhou *et al.* 2018), carbon nanofibers (Wang *et al.* 2012), graphene (Dong *et al.* 2014), metal-organic framework-derived carbon materials (Ma *et al.* 2019), and carbon aerogels (Liu *et al.* 2020) have been widely studied. Most of these materials are energy-intensive and synthesized from expensive resources, so high-performance electrode materials based on wastes or recycled products with abundant resources should be developed.

Unwanted waste-derived carbons are ideal alternatives because they are cost efficient and environmentally friendly (Idrees *et al.* 2020; Teong *et al.* 2020; Wu *et al.* 2020). Paper waste (Pham *et al.* 2020), sewage sludge ash (Wang *et al.* 2019), cotton waste (Sartova *et al.* 2019), and paper mill sludge (Jaria *et al.* 2019) have been proven useful in various applications. Nearly six trillion cigarettes are consumed annually, which leads to about 800,000 metric tons of waste cigarette butts. They are non-biodegradable and exert a tremendous impact on environmental and biological health (Blankenship & Mokaya 2017). Extensive efforts have been made to effectively transform waste cigarette butts into suitable porous carbon materials. Li and co-workers prepared cigarette-derived functional carbon materials that had bifunctional applications in supercapacitors and water contaminant removal (Li *et al.* 2020). Blankenship and Mokaya showed that porous carbons derived from cigarette butts have ultra-high surface areas (4,300 $m^2 g^{-1}$) and exhibit unprecedentedly high hydrogen storage capacity (Blankenship & Mokaya 2017). Li's group fabricated hierarchical porous sorbents combined with the high adsorption capability of the mesopores and the shape-selectivity of the micropores using waste cigarette butts as a starting material (Li *et al.* 2019). Hou and co-workers recycled waste cigarette butts for sodium-ion batteries (SIB) and demonstrated their high electrochemical Na-storage performance (Hou *et al.* 2019). It was confirmed that cigarette butt-derived carbon has a large specific surface area, abundant pore structure, and large ion storage capacity (Chang *et al.* 2015; Meng *et al.* 2019; Xiong *et al.* 2019), which are highly desirable for CDI. Therefore, we prepared cigarette butt-derived carbon materials and applied them to CDI. Two current methods for the preliminary carbonization of cigarette butts are high-temperature carbonization and hydrothermal carbonization (Blankenship & Mokaya 2017). High-temperature carbonization requires considerable energy and time to raise and lower the temperature. Hydrothermal carbonization requires the cigarette butts to be placed in a reaction kettle, which uses the high pressure in the closed space during the reaction to perform low-temperature carbonization and obtain a carbon-containing precursor with high porosity (Lee & Park 2021). This makes it more feasible in preparing CDI electrode materials. There are two types of activation methods, physical activation (Bazan-Wozniak *et al.* 2021) and chemical activation (Olivares-Marín *et al.* 2006). The chemical activation process is more stable, mature, and suitable for large-scale production compared with the former.

Here, we synthesized smoked cigarette butt-derived carbon (SCC) by hydrothermal carbonization and chemical activation with three activation temperatures (650, 750 and 850 °C). We also investigated the electrochemical properties of these materials and the performance for desalination in CDI. Unsmoked cigarette butt-derived carbon at an activation temperature of 750 °C (UCC-750) was also synthesized for comparison.

2. EXPERIMENTAL SECTION

2.1. Materials

Smoked cigarette butts were collected from public places in Shanghai and unsmoked cigarette butts were purchased from Shandong China Tobacco Industry Co., Ltd. All chemicals were of analytical reagent grade and used without further purification. Carbon black (325 mesh) was obtained from Lion Corporation (Japan). The graphite sheet was purchased from the Tianqi Lithium Corp Company (Shanghai, China). Sodium hydroxide, hydrochloric acid (36–38%), polyvinylidene fluoride, *N*-methyl-2-pyrrolidone, and sodium chloride were purchased from Sinopharm Chemical Reagent Co., Ltd.

2.2. Synthesis of porous carbon from the cigarette butt

Figure 1 shows the synthesis procedure of the cigarette butt-derived carbon material. The outside of the cigarette butt (wrapping paper, ash, impurities) was removed first and cut into several segments. A mixture of 0.5 g of cigarette butts with 50 mL deionized water was hydrothermally carbonized by heating at 250 °C for two hours in a para-polyphenol (PPL) liner and cooled to room temperature. The sediments were washed several times until the upper liquid was clear and dried at 112 °C overnight to obtain the precursor. We prepared a fully ground mixture of KOH/precursor with a 4:1 ratio for chemical activation. This mixture was heated to 650, 750, or 850 °C at a ramping rate of 3 °C min^{-1} for an hour and cooled under nitrogen. Then 2 M HCl was used to wash the samples at room temperature until the pH of the liquid was neutral. Cigarette butt-derived carbon was recovered after being dried in an oven at 112 °C for six hours. The smoked and unsmoked cigarette butt-derived carbon was named SCC-T and UCC-T, respectively, where T is the activation temperature (650, 750 or 850 °C).

2.3. Preparation of the electrodes

The synthesized porous carbon, PVDF dissolved in NMP, and carbon black powder were mixed at a ratio of 8:1:1 to obtain a homogeneous slurry. This slurry was cast onto a 1×2 cm graphite sheet for the electrochemical characterization and a 3.5×3 cm graphite sheet for the CDI performance test and dried at 60 °C for 10 hours. The final thickness of the electrode was 200 μm.

2.4. Characterization

Scanning electron microscopy (SEM, Sigma 500, Germany) was used to observe the surface morphology of the materials. The defect degree of the samples was recorded using a laser Raman spectrometer (HORIBA LabRAM HR Evolution, France). X-ray diffraction (XRD, Smartlab9, Japan) was used to analyze the crystalline structures of the samples. The surface area was calculated from the N_2 isotherms, which were measured by an Autosorb-iQ2-MP analyzer and fitted using the Brunauer–Emmett–Teller (BET) method. The pore size distribution (PSD) was obtained by density functional theory (DFT) fitting of the N_2 isotherms. The electrochemical behavior of the materials was characterized by an electrochemical workstation (Autolab PGSTAT302N, Metrohm Instruments Inc, Switzerland). The analytical electrochemical methods employed were

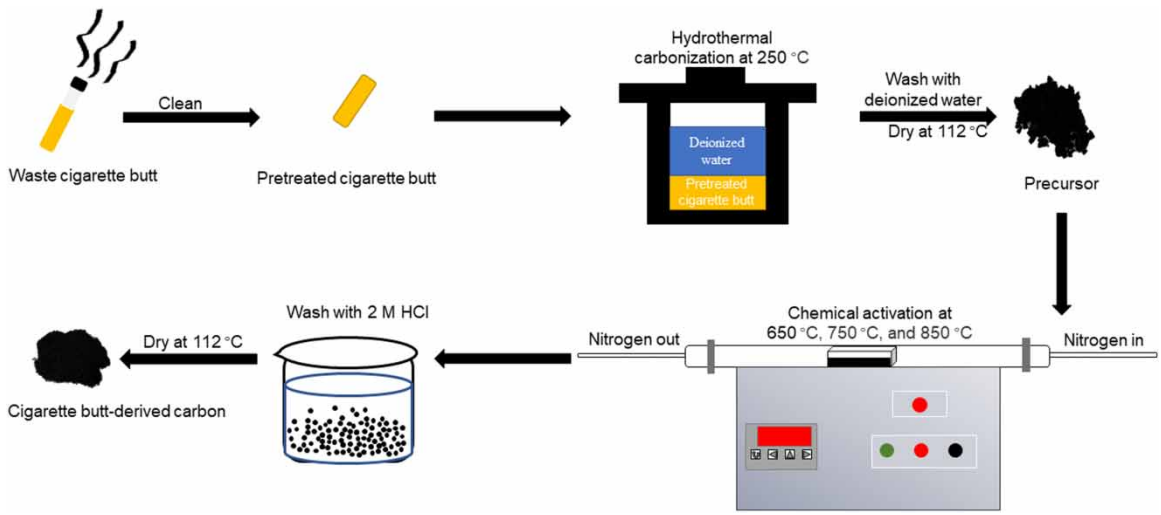

Figure 1 | The schematic diagram of the experimental procedure.

cyclic voltammetry (CV), galvanostatic charging/discharging (GCD), and electrochemical impedance spectroscopy (EIS). These measurements were conducted in a conventional three-electrode cell in a 6 M NaOH solution. The Pt and Hg/HgCl electrodes were used as the counter and reference electrodes, respectively.

The specific capacitance (C, F g^{-1}) was calculated according to Equation (1).

$$C = (I\Delta t)/(m\Delta V) \tag{1}$$

Here, I is the discharge current in amps, Δt is the discharge time in seconds, m is the mass of electrode active materials in grams, and ΔV is the voltage change in volts.

2.5. Batch mode CDI tests

The desalination experiment was operated in batch mode with five pairs of electrodes assembled in a rectangular chamber as shown in Figure 2. The dimension of each electrode is 3 × 3.5 cm with a 1 × 1 mm hole in the middle. Adjacent electrodes were separated by a 500 μm thick spacer with the space porosity of 93.58% to prevent short-circuited. The NaCl solution was pumped through the CDI cell with a peristaltic pump (YZ1515, Longer Inc., Shanghai). The conductivity change of the NaCl solution was monitored by an online conductivity meter (PDSJ-308A, Lei-Ci Instruments Inc., Shanghai) at the CDI outlet. The relationship between conductivity and concentration was obtained according to a calibration curve. The NaCl solution concentrations used in the experiments were 600, 800, and 1,000 mg L^{-1} with a total water volume of 30 mL in the system. The applied potential differences were 0.8, 1.0, and 1.2 V for the charging step and 0 V for the discharging step (each step for 30 min). The salt adsorption capacity, (SAC, Γ, mg g^{-1}), charge (Σ, c g^{-1}), and charge efficiency(Λ) are given by Equations (2)–(4).

$$\Gamma = \frac{(C_0 - C)V}{m} \tag{2}$$

$$\Sigma = \int i\frac{dt}{m} \tag{3}$$

$$\Lambda = \Gamma \cdot \frac{F}{\Sigma \cdot M} \tag{4}$$

Here, C_0 and C are the initial and final NaCl concentrations in mg L^{-1}, respectively, V is the NaCl solution volume in L, and m refers to the total mass of the carbon materials in g. Additionally, i represents the absolute value of the electrical

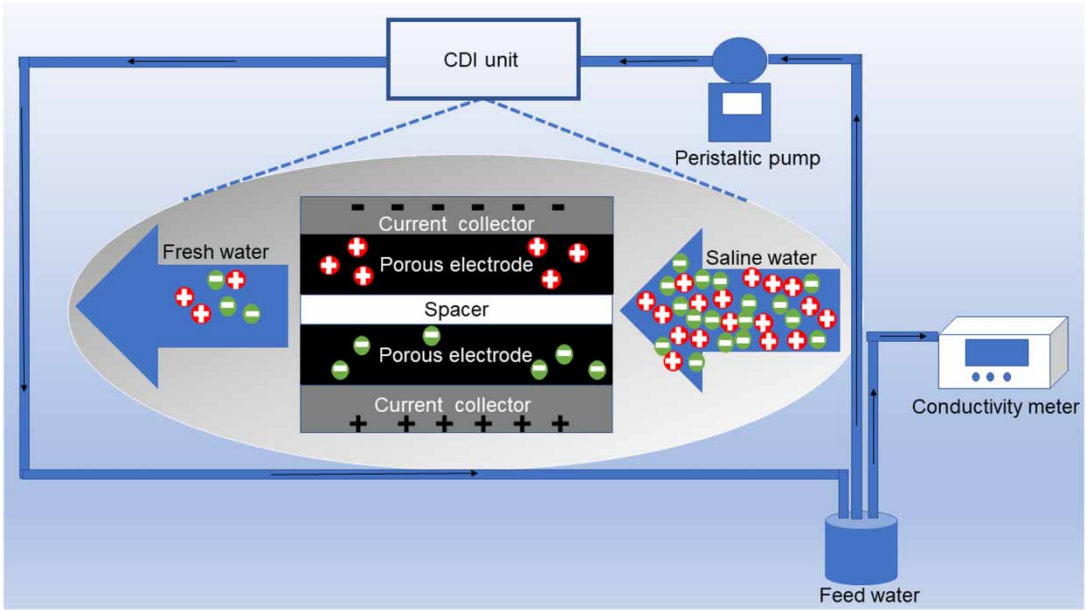

Figure 2 | The schematic diagram of the CDI model.

current during either the adsorption or the desorption step in amps over a time, t, in min. F is the Faraday constant (96,485 C mol^{-1}) and M is the molar weight of NaCl (58.44 g mol^{-1}).

3. RESULTS AND DISCUSSION

3.1. Morphology and structural characterization

The SEM images of the samples are shown in Figure 3(a)–3(d). They all demonstrate a three-dimensional structure with abundant pores of different sizes. SCC exhibits a closer honeycomb-like structure compared to unsmoked cigarette butt-derived carbon as shown in Figure 3(b)–3(d). The pore area becomes slightly larger with the increase of the activation temperature, which is shown in Table 1.

Samples were degassed at 200 °C for 15 hours for the pretreatment before the nitrogen isothermal adsorption and desorption experiments. As shown in Figure 4(a), all samples are type I isotherms except SCC-750. The adsorption capacity rises rapidly in the low-pressure area (P_0, $P^{-1} < 0.1$) revealing the presence of a large number of micropores, which help

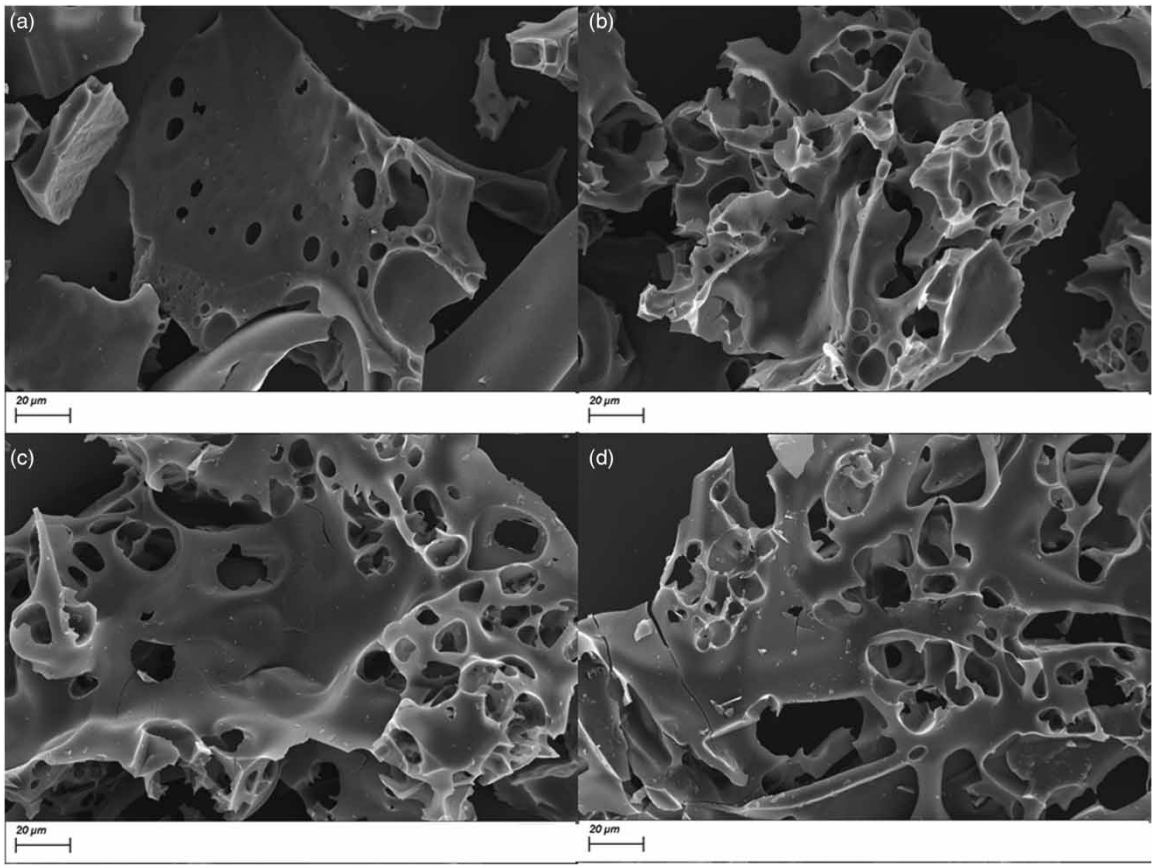

Figure 3 | The SEM images (a)–(d) of UCC-750, SCC-650, SCC-750, and SCC-850.

Table 1 | Pore structure characteristic properties of UCC-750 and SCC samples

Samples	S_{BET} ($m^2\ g^{-1}$)	S_{micro} ($m^2\ g^{-1}$)	V_{total} ($cm^3\ g^{-1}$)	V_{micro} ($cm^3\ g^{-1}$)	V_{mic}/V_t (%)	S_{micro}/S_{BET} (%)	D_{ave} (nm)
UCC-750	2,376.96	2,156.09	1.20	0.98	81.59	90.70	2.01
SCC-650	2,680.19	2,488.43	1.34	1.15	85.38	92.85	2.00
SCC-750	3,093.10	2,707.13	1.75	1.39	78.96	87.52	2.27
SCC-850	2,994.77	2,788.78	1.53	1.32	86.17	93.12	2.04

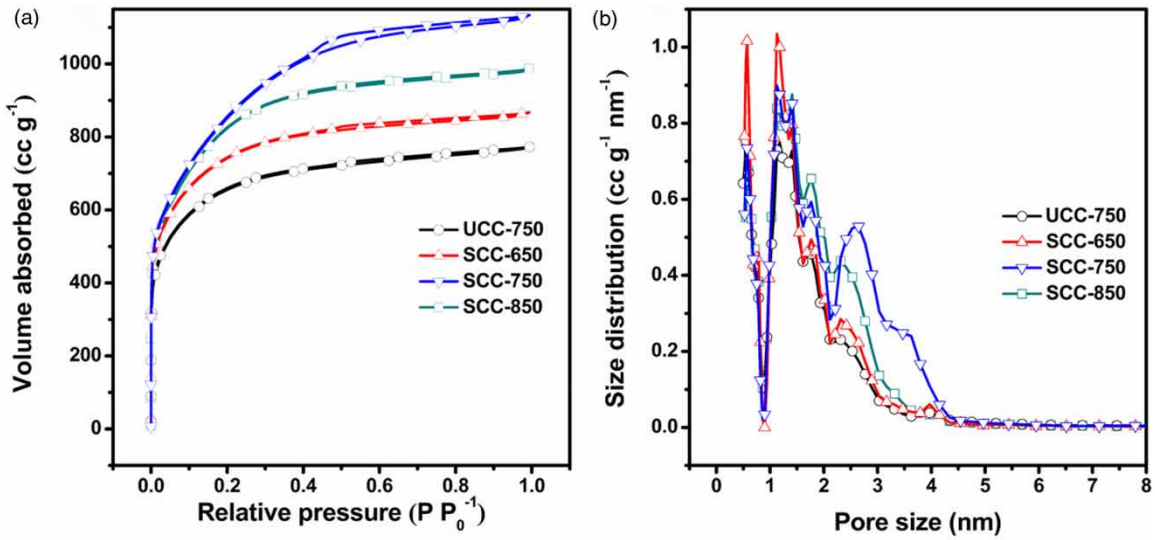

Figure 4 | (a) N_2 adsorption/desorption isotherms and (b) DFT pore size distributions of UCC-750, SCC-650, SCC-750, and SCC-850.

to increase the specific capacitance (Chmiola *et al.* 2006; Huang *et al.* 2011). The nitrogen adsorption isotherm of SCC-750 is type IV. There is an obvious adsorption hysteresis loop in the medium pressure area (P_0, $P^{-1} = 0.1–0.9$), implying that the sample is rich in mesopores. The PSDs of the samples are in Figure 4(b), where it is shown that all samples display a bimodal pore structure with micropores ranging from 0.5 to 2 nm and mesopores between 2 and 4.5 nm. Such a pore structure increases the specific surface area and the adsorption/transmission of ions (Fernández *et al.* 2009). UCC-750, SCC-650, and SCC-850 possess more micropores than mesopores, as shown in Figure 4(b), while SCC-750 shows a rise in mesopore distribution with pore sizes ranging from 2 to 3 nm. Table 1 lists the detailed pore structure parameters of all samples. All SCC materials have larger SSA and higher pore volumes compared with UCC materials, whereas more pores are observed from the SCC materials. This is confirmed in the SEM images. This is likely to be due to the impurities from the smoked cigarette butts that could create a porous structure during the degradation process (Li *et al.* 2019). SCC-750 has the highest BET area (3,093.10 $m^2 g^{-1}$) and highest total pore volume (1.75 $cm^3 g^{-1}$) compared with other SCC materials fabricated at 650 °C and 850 °C, which implies that it is difficult to generate the micropores at the low temperature. There is an increase in the micropore

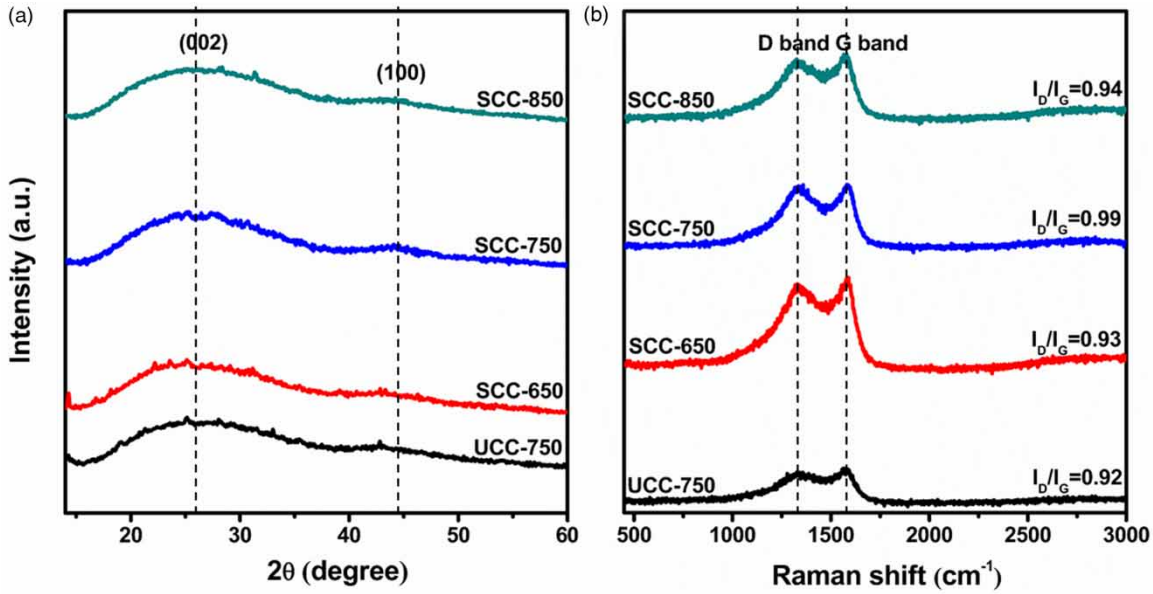

Figure 5 | (a) XRD pattern and (b) Raman spectra of UCC-750, SCC-650, SCC-750, and SCC-850.

area at 850 °C and the higher temperature also leads to the loss of the mesopores, as shown in Figure 4(b). The mesopores are considered to be important for the ion transportation of the deionization processes (Dykstra *et al.* 2016). Therefore, SCC-750, with the highest mesopore area, also exhibits the best electrochemical performance, as discussed in section 3.2.

XRD and Raman spectroscopy were carried out to investigate the inner structures of the samples. The dashed line is to guide the eye. All samples have a (002) peak centered at $2\theta = 26^{o}$ that originates from the interlayer space between carbon layers as shown in Figure 5(a). This peak indicates the random orientation of aromatic carbon sheets in amorphous carbon, which can stimulate structural disorder and increase the specific surface area (Zhao *et al.* 2016). There is a weak peak at $2\theta = 44^{o}$ representing the (100) diffraction mode of the graphitic structure. The Raman spectra are shown in Figure 5(b). Two peaks at 1,320 and 1,565 cm^{-1} are observed, which correspond to the D band (defect-induced band) and G band (crystalline graphite band), respectively. The intensity ratio of the D peak to G peak (I_D/I_G) is widely accepted as a parameter to measure the defect degree of carbon materials (Zoromba *et al.* 2017). These ratios of the as-prepared materials ranged from 0.92 to 0.99, suggesting relatively high defect density, and SCC-750 had the highest ratio among the samples. The high defect degree is important to increase the surface area and the pore volumes.

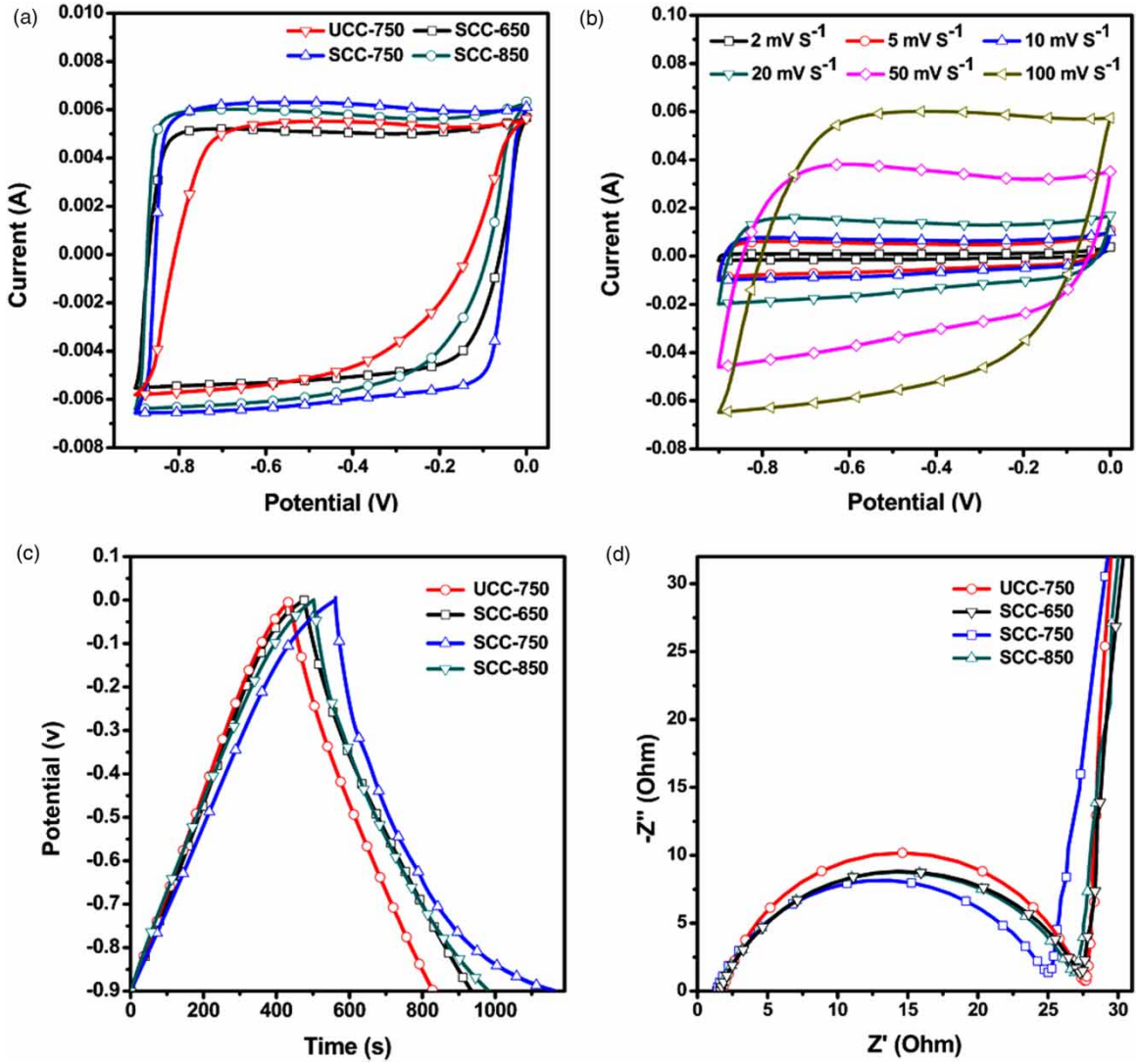

Figure 6 | (a) CV curves of UCC-750, SCC-650, SCC-750, and SCC-850 electrodes at a 10 mV s^{-1} scan rate. (b) CV curves of the SCC-750 electrode at different scan rates (2, 5, 10, 20, 50, and 100 mV s^{-1}). (c) GCD curves of UCC-750, SCC-650, SCC-750, and SCC-850 electrodes at a current density of 0.3 A g^{-1}. (d) Nyquist profiles of UCC-750, SCC-650, SCC-750, and SCC-850 electrodes.

3.2. Electrochemical characterization

Figure 6(a) shows the CV plots of the UCC-750 and SCC electrodes at different activation temperatures in an electrical potential window between −0.9 and 0 V. All CV curves exhibit quasi-rectangular features and there are no evident redox peaks. This suggests a representative EDL capacitance behavior without pseudo-capacitance. The integral area under the CV curves represents the specific capacitance (Meng *et al.* 2019). All SCC electrodes have a larger integral area than the UCC-750 electrode, which is due to the SCC electrode's larger BET area. The SCC-750 electrode has the largest integral area of all CV measurements, suggesting the highest specific capacitance. All the CV curves of the SCC-750 electrode keep their shape even at a 100 mV s^{-1} scan rate, indicating a good performance rate, as shown in Figure 6(b).

The GCD curves of UCC-750, SCC-650, SCC-750, and SCC-850 electrodes are all nearly triangular, which suggests a good reversibility and ideal electrical double-layer capacitance, as shown in Figure 6(c). Longer charging/discharging times reflect higher specific capacitance [51] and this can be calculated quantitatively according to Equation (1). The results of UCC-750, SCC-650, SCC-750, and SCC-850 electrodes are 130.80, 152.57, 201.09, and 160.31 F g^{-1}, respectively. The SCC-750 electrode has the largest specific capacitance, which agrees with the CV results. This is because the SCC-750 electrode has high porosity and specific surface area (Table 1) providing well developed pore channels for ion transmission, which is highly desired for CDI applications. The GCD tests were also conducted in 1 M and 2 M KOH solutions to compare the specific capacitance with the currently published cigarette butt-derived carbon electrode and commercial activated carbon electrode. The results are summarized in Figure 7 with the specific capacitance from this work indicated by a dashed line, which demonstrates that the SCC-750 electrode's performance is improved over these materials.

Figure 6(d) shows the EIS plot of all the electrodes. they all shape a slope line at low frequency and a small quasi-semicircle at high frequency. The first intersection of the curve and Z′ corresponds to the equivalent series resistances (ESRs). The diameter of the semicircle represents the charge transfer resistance. The SCC-750 electrode has the smallest ESRs and the diameter of the semicircle is smaller than the other electrodes, which implies its faster charge transfer.

3.3. CDI performance

A series of CDI tests was carried out to verify the desalination performance of the SCC-750 electrode and electrodes from unsmoked cigarette butts. The Na^+ and Cl^- are separately adsorbed into their opposite electrodes and the salt concentrations and conductivity decrease when applying a voltage over the electrodes. The electrosorption process reaches equilibrium after

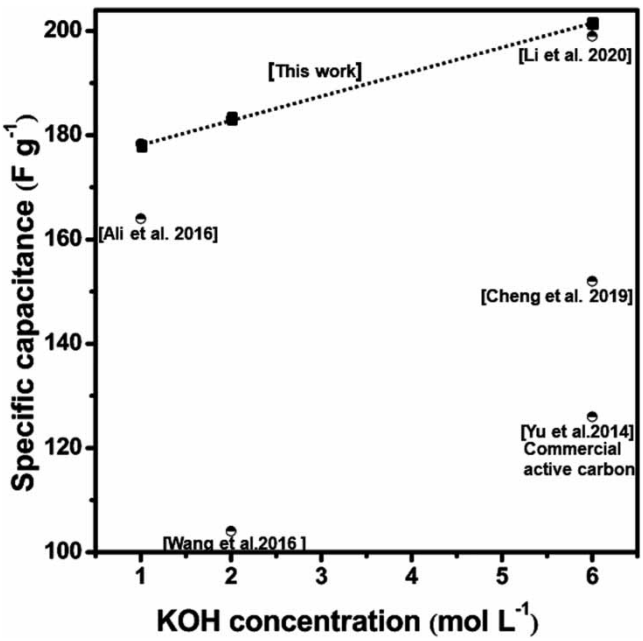

Figure 7 | Specific capacitance comparison of commercial activated carbon and carbon materials derived from cigarette butts in KOH solutions. Squares are from this work and circles are from previous works (Yu *et al.* 2014; Ali *et al.* 2016; Wang *et al.* 2016; Cheng *et al.* 2019; Li *et al.* 2020).

30 min. Then, during the discharging step, the CDI cell is short-circuited to release ions. The conductivity changes of the UCC-750 and SCC-750 electrodes are shown in Figure 8(a). The SCC-750 electrode exhibits a larger conductivity change compared to the UCC-750 electrode during charging step and discharging step, which is due to its porous inner structure and excellent electrochemical performance. An increased conductivity change was observed with an increased charging voltage, indicating that more ions were absorbed and released as shown in Figure 8(b). This is because a higher voltage leads to larger electrostatic interactions and creates a thicker EDL (Sriramulu *et al.* 2019) where the Na^+ and Cl^- can transfer faster from the NaCl solution to the cigarette-derived carbon electrode surface. Capacitive performance can be boosted as a result.

The calculations of the electrosorption capacity and charge efficiency of the SCC-750 electrode with different initial NaCl concentrations are shown in Figure 8(c). The electrosorption capacities increased from 8.95 mg g^{-1} to 10.27 mg g^{-1} and the charge efficiencies increased from 0.34 to 0.43 when the initial NaCl concentrations increased from 600 to 1,000 mg L^{-1}, which suggests that higher initial NaCl concentrations result in better electrosorption capacity. The compression of the EDL is more intense and the effect of the double-layer overlap decreases (Shen *et al.* 2021). This enables faster ion

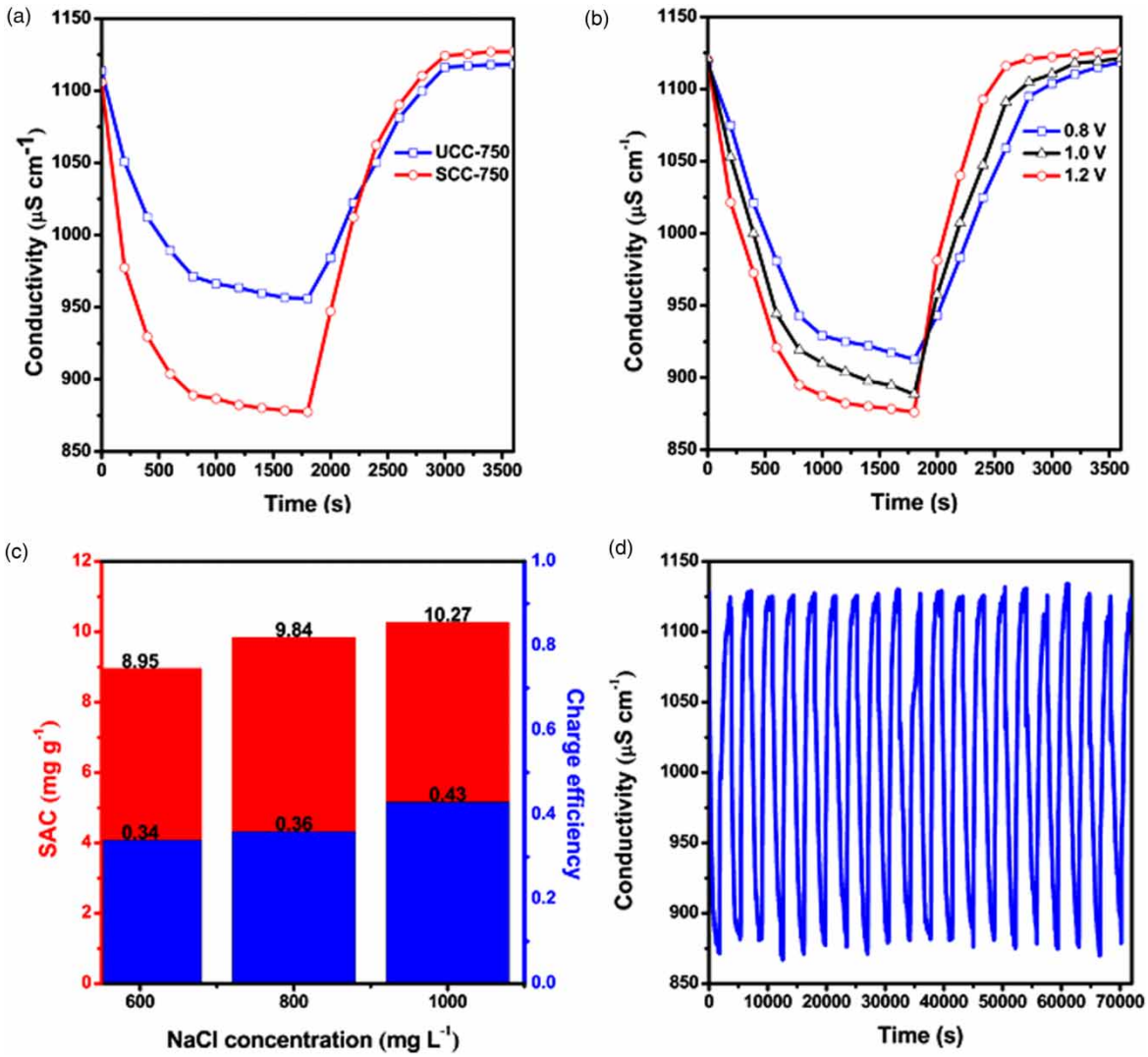

Figure 8 | (a) Desalination performance in a NaCl solution with an initial concentration of 600 mg L^{-1} for UCC -750, and SCC-750 electrodes at an applied charging voltage of 1.2 V. (b) Desalination performance in a NaCl solution with an initial concentration of 600 mg L^{-1} for the SCC-750 electrode at different charging voltages. (c) The electrosorption capacities (left axis) and charge efficiencies (right axis) of the SCC-750 electrode at different initial NaCl concentrations with a charging voltage of 1.2 V. (d) Repetitive electrosorption experiment for the SCC-750 electrode in a 600 mg L^{-1} NaCl solution with a charging voltage of 1.2 V and discharging voltage −1.2 V.

transmission and leads to higher deionization capacity at higher initial concentrations. The repetitive CDI tests were carried out to further investigate the regeneration performance, as shown in Figure 8(d). The SCC-750 electrode shows no obvious decline in desalination performance after 20 cycles of 1.2 V charge/−1.2 V discharge in a 600 mg L^{-1} NaCl solution, indicating a good regeneration performance.

4. CONCLUSION

We recycled non-biodegradable cigarette butt waste into a three-dimensional porous activated carbon material after carbonization and chemical activation for CDI applications. The carbon derived from smoked cigarette butts showed better morphologic and electrochemical performance compared with unsmoked cigarette butt-derived carbon. The desalination capacity was improved by smoking the cigarette, which is ideal because smoked cigarette butts are more toxic and accessible. The activation temperature was proven to have an influence on the performance of the as-prepared electrode. The SCC-750 electrode exhibited the highest specific surface area (3,093.10 $m^2\ g^{-1}$), the highest pore volume (1.75 $cm^3\ g^{-1}$), and a suitable micro/mesopore distribution among all samples, which led to high specific capacitance (201.09 F g^{-1}). Therefore, the SCC-750 electrodes achieved a high SAC (10.27 mg g^{-1}) in a 1,000 mg L^{-1} NaCl solution at 1.2 V and was reversible even after 20 cycles of CDI experiments. This work provides a new and effective method of tackling environmental pollution concerning cigarette butts and promotes the development of electrode materials for CDI application.

ACKNOWLEDGEMENT

This work was supported by the National Natural Science Foundation of China (NSFC: 21606085).

DATA AVAILABILITY STATEMENT

All relevant data are included in the paper or its Supplementary Information.

REFERENCES

Ali, Z., Tahir, M., Cao, C., Mahmood, A., Mahmood, N., Butt, F. K., Tanveer, M., Shakir, I., Rizwan, M., Idrees, F., Aslam, I. & Zou, J.-J. 2016 Solid waste for energy storage material as electrode of supercapacitors. *Materials Letters* **181**, 191–195.

Anderson, M. A., Cudero, A. L. & Palma, J. 2010 Capacitive deionization as an electrochemical means of saving energy and delivering clean water. Comparison to present desalination practices: will it compete? *Electrochimica Acta* **55** (12), 3845–3856.

Asquith, B. M., Meier-Haack, J. & Ladewig, B. P. 2015 Poly(arylene ether sulfone) copolymers as binders for capacitive deionization activated carbon electrodes. *Chemical Engineering Research and Design* **104**, 81–91.

Bazan-Wozniak, A., Nowicki, P. & Pietrzak, R. 2021 Removal of NO_2 from gas stream by activated bio-carbons from physical activation of residue of supercritical extraction of hops. *Chemical Engineering Research and Design* **166**, 67–73.

Biesheuvel, P. M., Zhao, R., Porada, S. & van der Wal, A. 2011 Theory of membrane capacitive deionization including the effect of the electrode pore space. *Journal of Colloid and Interface Science* **360** (1), 239–248.

Blankenship, T. S. & Mokaya, R. 2017 Cigarette butt-derived carbons have ultra-high surface area and unprecedented hydrogen storage capacity. *Energy & Environmental Science* **10** (12), 2552–2562.

Chang, B., Guo, Y., Li, Y. & Yang, B. 2015 Hierarchical porous carbon derived from recycled waste filter paper as high-performance supercapacitor electrodes. *RSC Advances* **5** (88), 72019–72027.

Cheng, Y., Zhang, Q., Fang, C., Huang, Z., Chen, J., Wu, L. & Wang, H. 2019 Synthesis of N-doped porous carbon materials derived from waste cellulose acetate fiber via urea activation and its potential application in supercapacitors. *Journal of the Electrochemical Society* **166** (6), A1231–A1238.

Chmiola, J., Yushin, G., Gogotsi, Y., Portet, C., Simon, P. & Taberna, P. L. 2006 Anomalous increase in carbon capacitance at pore sizes less than 1 nanometer. *Science* **313** (5794), 1760–1763.

Dong, Q., Wang, G., Qian, B., Hu, C., Wang, Y. & Qiu, J. 2014 Electrospun composites made of reduced graphene oxide and activated carbon nanofibers for capacitive deionization. *Electrochimica Acta* **137**, 388–394.

Dykstra, J. E., Zhao, R., Biesheuvel, P. M. & van der Wal, A. 2016 Resistance identification and rational process design in capacitive deionization. *Water Research* **88**, 358–370.

Fernández, J. A., Tennison, S., Kozynchenko, O., Rubiera, F., Stoeckli, F. & Centeno, T. A. 2009 Effect of mesoporosity on specific capacitance of carbons. *Carbon* **47** (6), 1598–1604.

Gao, Y., Li, Z., Fu, Z., Zhang, H., Wang, G. & Zhou, H. 2021 Highly selective capacitive deionization of copper ions in FeS2@N, S co-doped carbon electrode from wastewater. *Separation and Purification Technology* **262**, 118336.

Ghaffour, N., Missimer, T. M. & Amy, G. L. 2013 Technical review and evaluation of the economics of water desalination: current and future challenges for better water supply sustainability. *Desalination* **309**, 197–207.

He, F., Biesheuvel, P. M., Bazant, M. Z. & Hatton, T. A. 2018 Theory of water treatment by capacitive deionization with redox active porous electrodes. *Water Research* **132**, 282–291.

Hou, H., Yu, C., Liu, X., Yao, Y., Dai, Z. & Li, D. 2019 The effect of carbonization temperature of waste cigarette butts on Na-storage capacity of N-doped hard carbon anode. *Chemical Papers* **73** (5), 1237–1246.

Hou, C., Wen, Y., Liu, X. & Dong, M. 2021 Impacts of regional water shortage information disclosure on public acceptance of recycled water – evidences from China's urban residents. *Journal of Cleaner Production* **278**, 123965.

Huang, W., Zhang, H., Huang, Y., Wang, W. & Wei, S. 2011 Hierarchical porous carbon obtained from animal bone and evaluation in electric double-layer capacitors. *Carbon* **49** (3), 838–843.

Idrees, M., Ahmed, S., Mohammed, Z., Korivi, N. S. & Rangari, V. 2020 3D printed supercapacitor using porous carbon derived from packaging waste. *Additive Manufacturing* **36**, 101525.

Jaria, G., Calisto, V., Silva, C. P., Gil, M. V., Otero, M. & Esteves, V. I. 2019 Obtaining granular activated carbon from paper mill sludge – a challenge for application in the removal of pharmaceuticals from wastewater. *Science of the Total Environment* **653**, 393–400.

Jia, B. & Zhang, W. 2016 Preparation and application of electrodes in capacitive deionization (CDI): a state-of-art review. *Nanoscale Research Letters* **11** (1), 64.

Lee, J. & Park, K. Y. 2021 Conversion of heavy metal-containing biowaste from phytoremediation site to value-added solid fuel through hydrothermal carbonization. *Environmental Pollution* **269**, 116127.

Li, S., Shi, C. L., Wang, Y.-Z., Sun, X. D., Qi, D.-W., Wu, D., Wang, Y. & Zhu, J. 2019 New efficient selective adsorbent of tobacco specific nitrosamines derived from discarded cigarette filters. *Microporous and Mesoporous Materials* **284**, 393–402.

Li, L., Jia, C., Zhu, X. & Zhang, S. 2020 Utilization of cigarette butt waste as functional carbon precursor for supercapacitors and adsorbents. *Journal of Cleaner Production* **256**, 120326.

Li, Z., Mao, S., Yang, Y., Sun, Z. & Zhao, R. 2021 Controllable synthesis of a hollow core-shell Co-Fe layered double hydroxide derived from Co-MOF and its application in capacitive deionization. *Journal of Colloid and Interface Science* **585**, 85–94.

Liu, Y., Zhang, X., Gu, X., Wu, N., Zhang, R., Shen, Y., Zheng, B., Wu, J., Zhang, W., Li, S. & Huo, F. 2020 One-step turning leather wastes into heteroatom doped carbon aerogel for performance enhanced capacitive deionization. *Microporous and Mesoporous Materials* **303**, 110303.

Ma, X., Chen, Y.-A., Zhou, K., Wu, P.-C. & Hou, C.-H. 2019 Enhanced desalination performance via mixed capacitive-Faradaic ion storage using RuO_2-activated carbon composite electrodes. *Electrochimica Acta* **295**, 769–777.

Mao, S., Chen, L., Zhang, Y., Li, Z., Ni, Z., Sun, Z. & Zhao, R. 2019 Fractionation of mono- and divalent ions by capacitive deionization with nanofiltration membrane. *Journal of Colloid and Interface Science* **544**, 321–328.

Meng, Q., Chen, W., Wu, L., Lei, J., Liu, X., Zhu, W. & Duan, T. 2019 A strategy of making waste profitable: nitrogen doped cigarette butt derived carbon for high performance supercapacitors. *Energy* **189**, 116241.

Naimi Ait-Aoudia, M. & Berezowska-Azzag, E. 2016 Water resources carrying capacity assessment: the case of Algeria's capital city. *Habitat International* **58**, 51–58.

Olivares-Marín, M., Fernández-González, C., Macías-García, A. & Gómez-Serrano, V. 2006 Preparation of activated carbon from cherry stones by chemical activation with ZnCl2. *Applied Surface Science* **252** (17), 5967–5971.

Pham, T. H., Jung, S. H., Kim, Y. J. & Kim, T. 2020 Adsorptive removal and recovery of organic pollutants from wastewater using waste paper-derived carbon-based aerogel. *Chemosphere* **268**, 129319.

Porada, S., Zhao, R., van der Wal, A., Presser, V. & Biesheuvel, P. M. 2013 Review on the science and technology of water desalination by capacitive deionization. *Progress in Materials Science* **58** (8), 1388–1442.

Sartova, K., Omurzak, E., Kambarova, G., Dzhumaev, I., Borkoev, B. & Abdullaeva, Z. 2019 Activated carbon obtained from the cotton processing wastes. *Diamond and Related Materials* **91**, 90–97.

Shen, Y. Y., Wu, S. W. & Hou, C. H. 2021 Exploring the electrosorption selectivity and recovery of indium ions with capacitive deionization in acidic solution. *Journal of Colloid and Interface Science* **586**, 819–829.

Sriramulu, D., Vafakhah, S. & Yang, H. Y. 2019 Activated Luffa derived biowaste carbon for enhanced desalination performance in brackish water. *RSC Advances* **9** (26), 14884–14892.

Strathmann, H. 2010 Electrodialysis, a mature technology with a multitude of new applications. *Desalination* **264** (3), 268–288.

Suss, M. E., Porada, S., Sun, X., Biesheuvel, P. M., Yoon, J. & Presser, V. 2015 Water desalination via capacitive deionization: what is it and what can we expect from it? *Energy & Environmental Science* **8** (8), 2296–2319.

Sutcliffe, C., Knox, J. & Hess, T. 2021 Managing irrigation under pressure: how supply chain demands and environmental objectives drive imbalance in agricultural resilience to water shortages. *Agricultural Water Management* **243**, 106484.

Teong, C. Q., Setiabudi, H. D., El-Arish, N. A. S., Bahari, M. B. & Teh, L. P. 2020 Vatica rassak wood waste-derived activated carbon for effective Pb(II) adsorption: kinetic, isotherm and reusability studies. *Materials Today: Proceedings* **42**, 165–171.

Vafakhah, S., Beiramzadeh, Z., Saeedikhani, M. & Yang, H. Y. 2020 A review on free-standing electrodes for energy-effective desalination: recent advances and perspectives in capacitive deionization. *Desalination* **493**, 114662.

Vörösmarty, C. J., McIntyre, P. B., Gessner, M. O., Dudgeon, D., Prusevich, A., Green, P., Glidden, S., Bunn, S. E., Sullivan, C. A., Liermann, C. R. & Davies, P. M. 2010 Erratum: global threats to human water security and river biodiversity. *Nature* **468** (7321), 334–334.

Wang, G., Pan, C., Wang, L., Dong, Q., Yu, C., Zhao, Z. & Qiu, J. 2012 Activated carbon nanofiber webs made by electrospinning for capacitive deionization. *Electrochimica Acta* **69**, 65–70.

Wang, Y., Jiang, M., Yang, Y. & Ran, F. 2016 Hybrid electrode material of vanadium nitride and carbon fiber with cigarette butt/metal ions wastes as the precursor for supercapacitors. *Electrochimica Acta* **222**, 1914–1921.

Wang, Q., Li, J. S. & Poon, C. S. 2019 Using incinerated sewage sludge ash as a high-performance adsorbent for lead removal from aqueous solutions: performances and mechanisms. *Chemosphere* **226**, 587–596.

Wu, H. Y., Chen, S. S., Liao, W., Wang, W., Jang, M. F., Chen, W. H., Ahamad, T., Alshehri, S. M., Hou, C. H., Lin, K. S., Charinpanitkul, T. & Wu, K. C. 2020 Assessment of agricultural waste-derived activated carbon in multiple applications. *Environmental Research* **191**, 110176.

Xiong, Q., Bai, Q., Li, C., Li, D., Miao, X., Shen, Y. & Uyama, H. 2019 Nitrogen-doped hierarchical porous carbons from used cigarette filters for supercapacitors. *Journal of the Taiwan Institute of Chemical Engineers* **95**, 315–323.

Yu, S., Li, Y. & Pan, N. 2014 KOH activated carbon/graphene nanosheets composites as high performance electrode materials in supercapacitors. *RSC Advances* **4** (90), 48758–48764.

Zhang, C., He, D., Ma, J., Tang, W. & Waite, T. D. 2019a Comparison of faradaic reactions in flow-through and flow-by capacitive deionization (CDI) systems. *Electrochimica Acta* **299**, 727–735.

Zhang, Y., Chen, L., Mao, S., Sun, Z., Song, Y. & Zhao, R. 2019b Fabrication of porous graphene electrodes via CO_2 activation for the enhancement of capacitive deionization. *Journal of Colloid and Interface Science* **536**, 252–260.

Zhao, Y.-Q., Lu, M., Tao, P.-Y., Zhang, Y.-J., Gong, X.-T., Yang, Z., Zhang, G.-Q. & Li, H.-L. 2016 Hierarchically porous and heteroatom doped carbon derived from tobacco rods for supercapacitors. *Journal of Power Sources* **307**, 391–400.

Zhao, X., Wei, H., Zhao, H., Wang, Y. & Tang, N. 2020 Electrode materials for capacitive deionization: a review. *Journal of Electroanalytical Chemistry* **873**, 114416.

Zhou, F., Gao, T., Luo, M. & Li, H. 2018 Heterostructured graphene@$Na_4Ti_9O_{20}$ nanotubes for asymmetrical capacitive deionization with ultrahigh desalination capacity. *Chemical Engineering Journal* **343**, 8–15.

Zoromba, M. S., Abdel-Aziz, M. H., Bassyouni, M., Gutub, S., Demko, D. & Abdelkader, A. 2017 Electrochemical activation of graphene at low temperature: the synthesis of three-dimensional nanoarchitectures for high performance supercapacitors and capacitive deionization. *ACS Sustainable Chemistry & Engineering* **5** (6), 4573–4581.

First received 6 May 2021; accepted in revised form 11 June 2021. Available online 25 June 2021